Contents lists available at ScienceDirect

Tectonophysics

journal homepage: www.elsevier.com/locate/tecto

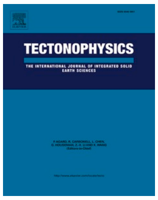

Monitoring induced seismicity in the Weiyuan shale gas field utilizing a dense array

Lichun Yang[d,1], Jinping Zi[b,c,1], Ruijia Wang[a,d,*], Hongfeng Yang[b,c,e,*]

[a] Shenzhen Key Laboratory of Deep Offshore Oil and Gas Exploration Technology, Southern University of Science and Technology, Shenzhen, Guangdong, China
[b] Shenzhen Research Institute, The Chinese University of Hong Kong, Shenzhen, Guangdong, China
[c] Department of Earth and Environmental Sciences, The Chinese University of Hong Kong, Shatin, Hong Kong, China
[d] Department of Earth and Space Sciences, Southern University of Science and Technology, Shenzhen, Guangdong, China
[e] Institute of Environment, Energy and Sustainability, The Chinese University of Hong Kong, Shatin, Hong Kong, China

ARTICLE INFO

Keywords:
Weiyuan shale gas field
Induced seismicity
Fluid migration
Seismicity detection and location

ABSTRACT

Understanding the mechanisms of induced seismicity and assessing associated hazards is crucial for risk mitigation in shale gas production regions. From August 2022 to February 2023, we maintained a dense array of 245 nodal stations with an average spacing of ~3 km, covering the entire Weiyuan shale gas field (WSGF), an actively exploited region that has experienced induced earthquakes up to M_w 5.0. Using the LOC-FLOW, we constructed a high-resolution earthquake catalog, precisely locating 29,669 events ranging from M_L −1.35 to M_L 3.42 with a completeness magnitude (M_c) of −0.24. Seismicity formed five distinct clusters, with those in the southern WSGF closely surrounding hydraulic fracturing wells and exhibiting migration patterns consistent with pore-pressure diffusion. In contrast, northern seismicity displayed characteristics of fault reactivation, with events aligning with pre-existing geological structures. Additionally, we observed persistent seismic activity near the epicenter of 2019 M_w 5.0 event, suggesting a long-lasting aftershock sequence. Our findings emphasize the necessity of high-resolution seismic monitoring and long-term hazard assessment in shale gas fields. The results contribute to a better understanding of injection-induced seismicity and fault activation processes, providing valuable insights for risk mitigation and sustainable resource production in tectonically sensitive regions.

1. Introduction

With the growing global demand for energy resources, shale gas has become an important energy supply to fulfill energy shortage. However, earthquake hazards associated with hydraulic fracturing (HF) during shale gas exploitation, with magnitudes up to M_s 6.0 (M_w 5.4; Zhao et al., 2023), threaten residents, properties, and operation safety. While substantial progress has been made in understanding induced seismicity mechanisms (e.g., Ellsworth, 2013; Schultz et al., 2020; Eyre et al., 2019; Moein et al., 2023; Yang et al., 2023), effective strategies in managing induced earthquake risks remain inadequate, largely due to unknown subsurface structures, complexities in triggering physics, and insufficient understanding of fault properties.

Deployment of temporary dense array became popular under variable induced settings (especially HF) for their advantages in obtaining high-resolution earthquake locations and subsurface structures (e.g., Wang et al., 2020; Tian et al., 2024; Eaton et al., 2018). For example, using a dense temporary array with an interstation of ~0.5 km, Zhang et al. (2022b) revealed detailed time-spatial seismicity migration and stress characteristics of HF induced earthquakes in the Western Canada Sedimentary Basin with relative location errors of meters. Aided by near-fault seismometers, Zi et al. (2025) revealed the 11-month long triggering processes in response to operations in multiple platforms presiding the 2019 Weiyuan M_w 5.0 earthquake with relative location errors less than 10 m. Tomography studies based on the dense array have been applied to reveal earthquake occurrence patterns (e.g. Zi et al., 2023; Li et al., 2023), pore pressure status (e.g., Tan et al., 2020; Tan et al., 2023) and structural features (e.g. Wei et al., 2022; Wang et al., 2024).

The Weiyuan shale gas field (WSGF), located within the Sichuan Basin (Fig. 1), bears the largest shale gas reserve in China. Since massive HF started in 2015, local seismicity quantity increased dramatically,

---

* Corresponding authors.
E-mail addresses: wangrj@sustech.edu.cn (R. Wang), hyang@cuhk.edu.hk (H. Yang).
[1] These authors contributed equally: Lichun Yang, Jinping Zi

https://doi.org/10.1016/j.tecto.2025.230862
Received 3 April 2025; Received in revised form 22 June 2025; Accepted 22 July 2025

including a number of destructive $M_w \geq 4.0$ earthquakes. Noteworthy instances include the February 2019 M_w 4.6 (M_L 4.9; Yang et al., 2020), which is the first deadly event triggered by HF, and the September 2019 M_w 5.0 earthquake (M_L 5.6; Zi et al., 2025) as one of the largest earthquakes triggered by HF worldwide.

With the ambition to comprehensively understand recent seismicity in the WSGF, we deployed a dense nodal array within ~80 km of Weiyuan. The array consists of 245 stations with four types of seismographs and was in operation from August 2022 to February 2023 (Figs. 1, 2). We constructed a high-resolution earthquake catalog including 29,669 events with a completeness magnitude (M_c) of −0.24. The temporal and spatial distribution of seismicity confirms the strong correlation between earthquakes and HF wells. Our findings provide critical insights into injection-induced earthquakes, fault activation processes, and long-term aftershock behavior, with implications for seismic hazard mitigation in shale gas fields.

2. Background

The WSGF is located in the southern Sichuan Basin (Fig. 1), with the Weiyuan anticline to the northwest as the main structural unit. The target fracking layer, the Upper Ordovician Wufeng Formation-Lower Silurian Longmaxi Formation, has burial depths ranging from ~1.5 km in the anticline to ~4.0 km toward the southeast (Ma et al., 2020). Over one hundred platforms have been established in the WSGF since mid-2015, and about half of them completed fracking and transitioned to the shale gas extraction stage after July 2022 (Fig. 1b).

So far, eight $M_w \geq 4.0$ events have struck the WSGF (Fig. 1b), six of which were located in southwestern Weiyuan, and the two largest events (M_w 5.0 and M_w 4.9) occurred in northeastern Weiyuan. Some destructive earthquakes are shallow and lead to observable coseismic surface deformation (Yang et al., 2020; Zhang et al., 2024a). Seismic reflection profiles reveal that the faults hosting these moderate earthquakes have limited offsets, challenging the identification of them before earthquakes occurrence (Liu et al., 2024; Liu et al., 2023a; Yang et al., 2020). Seismological observations (i.e., focal mechanisms) show that $M_L \geq 1.5$ events in the WSGF are dominated by reverse-faulting striking N-S (Chu and Sheng, 2023; Yi et al., 2020), consistent with the stress field estimated from borehole measurements (Chen et al., 2018).

Tomography studies suggest significant velocity heterogeneities in the study area (Zi et al., 2023; Du et al., 2021), where the locations of $M_L \geq 3.0$ events appear to be constrained by the Weiyuan anticline as well as the deep basement rift (Zi et al., 2023). Spatiotemporal analysis of small earthquakes associated with HF in the WSGF led to relatively high apparent fluid diffusion rates (i.e., 0.05–0.25 m^2/s; Zi et al., 2025; Yang et al., 2023; Sheng et al., 2022; Wang et al., 2023). Utilizing near-fault observations of the 2019 M_w 5.0 earthquake, Zi et al. (2025) reveals significant differences in source parameters (i.e., location, duration, and stress drop) between earthquakes directly associated with HF and those occurring on the hosting fault. Detailed analysis shows that the hosting fault undergoes 11-month precursory activation before the mainshock, emphasizing the importance of monitoring such activation for hazard mitigation.

3. Data and methods

3.1. Deployment of a dense temporary network

The dense network covers the entire WSGF (about 70 km × 80 km) with an average spacing of ~3 km (Fig. 2a) and was operational from August 2022 to February 2023. It was jointly deployed by a team of 15 members from The Chinese University of Hong Kong, Southern University of Science and Technology, and the Sichuan Earthquake Agency. The temporary dense array consists of 245 stations, including four types of short-period three-component seismographs (i.e., QS-05A, EPS-2-M6Q, TVG-63, and HR3C) from different manufacturers. To avoid

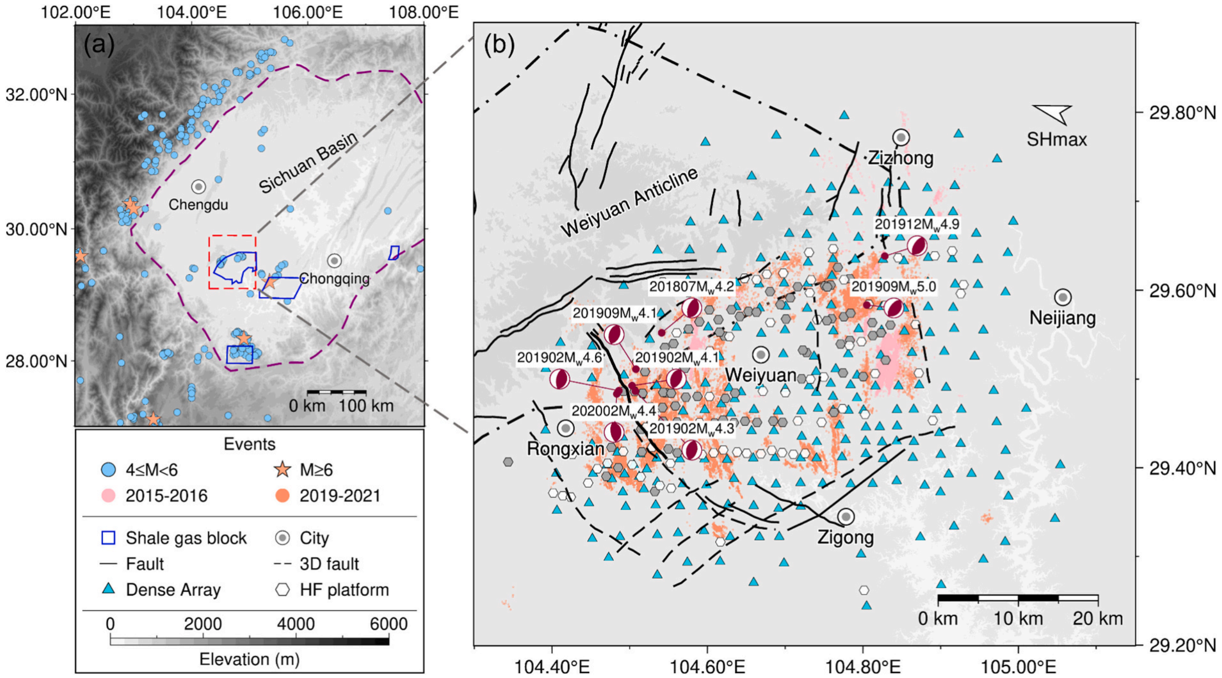

Fig. 1. (a) Map view of the Sichuan Basin with shale gas blocks (Lei et al., 2020), and reported earthquakes (M ≥ 4) between 2009 and 2024. (b) Map view of the Weiyuan shale gas field (WSGF). Beachballs are the focal mechanisms of M ≥ 4 events in the WSGF (Yi et al., 2020). The cyan triangles show 245 stations deployed from 2022 to 2023 in this study. Hydraulic fracturing platforms are plotted with filled gray (fracking completed in or before July 2022) and white (waiting for fracking) hexagons. The pink and orange dots are events from 2015 to 2016 (Sheng et al., 2022) and from 2019 to 2021 (Zi et al., 2023), respectively. The black solid and dashed lines represent mapped faults from geological survey and 3D seismic exploration, respectively (personal communication with Yang Zhao). The arrow of SHmax indicates the orientation of maximum horizontal stress (Lei et al., 2020). (For interpretation of the references to colour in this figure legend, the reader is referred to the web version of this article.)

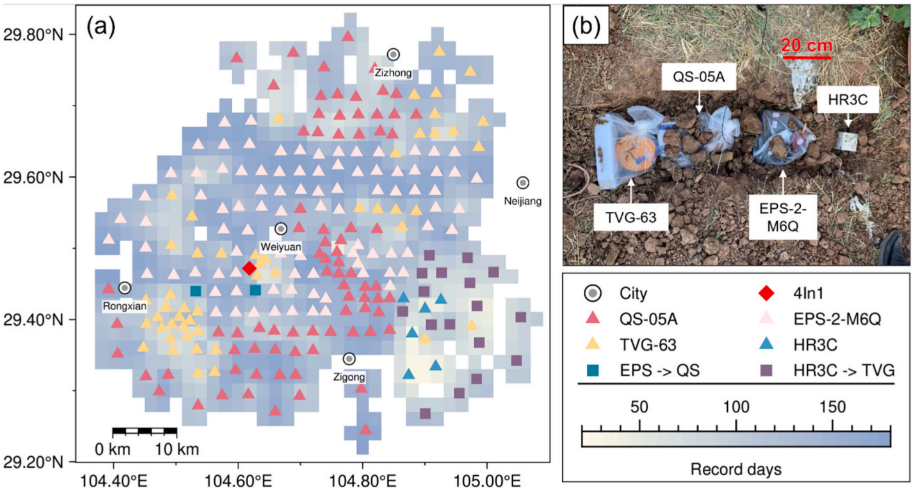

Fig. 2. (a) Spatial characteristic for instrument types and station recording times; (b) On-site photograph of station deployment ("4In1", red diamond) for instrument consistency testing. (For interpretation of the references to colour in this figure legend, the reader is referred to the web version of this article.)

potential bias from different instrument types and ensure waveform consistency, we reserved a "4In1" site that hosted four seismometers (Fig. 2b) from August 16 to November 5, 2022.

The built-in batteries for all types of nodal instruments only last for less than one month and external batteries were placed to extend the monitoring period to three months. To accomplish a 6-month coverage goal, we recharged stations and external batteries between November 5 and 13, 2022. During this period, we retrieved all HR3C instruments and redeployed TVG-63 instruments at 17 stations (purple squares in Fig. 2a). By the end, the dense temporary network achieved an average recording duration of 123 days per station, with the longest recording period reaching 178 days and the shortest being 23 days (i.e., HR3C without external battery). Spatially, stations situated near the Weiyuan region maintain consistent and reliable recording times, whereas those at the network's periphery show relatively shorter recording durations. Operating at a preset sampling rate of 250 Hz, these three-component geophones are well-suited for analyzing local seismic events, aseismic phenomena, and anthropogenic noise (Gu et al., 2024).

3.2. Phase picking and earthquake location

We employed LOC-FLOW to detect and locate earthquakes from continuous three-component waveforms (Zhang et al., 2022a). This state-of-the-art method has demonstrated its versatility and reliability in catalog construction across various spatial scales, ranging from regional to local, and has been applied in diverse contexts, including aftershock sequence analysis, microseismicity monitoring, and induced seismicity investigations (Zhang et al., 2025; Zhang et al., 2022b; Feng et al., 2024; Wang et al., 2023). In the following, we briefly present optimal parameters in each step.

First, we employed PhaseNet (Zhu and Beroza, 2018), a deep-neural-network-based phase picker, to detect P and S arrival times from continuous data. To achieve more accurate phase picking in southwestern Sichuan, we adopted a transfer-learned model (Zhao et al., 2021) trained on the dataset from the Sichuan Network. Finally, PhaseNet identified 417,5303 P and 351,8249 S phase arrival times with probabilities exceeding 0.4.

We then used a rapid earthquake association and location algorithm (i.e., REAL; Zhang et al., 2019) to associate the phase picks into events. We extracted the 1D velocity model from two regional 3D velocity models (Fig. S1): the shallow portion (<10 km) was averaged from the model in Zi et al. (2023), while the deeper portion (≥10 km) was obtained from SWChinaCVM-2.0 (Liu et al., 2023b). At this step, the search range was set to 0.3° horizontally and 15 km in depth, with grid intervals of 0.02° and 2 km, respectively. A successful event association requires at least 4 P phases, 3 S phases, 8 total phases (P + S), 3 common stations (i.e., detect P and S arrivals simultaneously), and travel time residual less than 0.4 s. Using these criteria, REAL initially associated and located 42,497 events (Figs. 3, 4a).

Both absolute earthquake location and double-difference relative location were applied to further refine event locations. Using HypoInverse (Klein, 2002), we obtained the absolute locations of 39,985 events with travel time residual <0.15 s and station gaps <210° (Fig. 4b). Both pick-derived and cross-correlation-derived differential times of these events were incorporated for the final relative relocation. We utilized FDTCC to accomplish rapid cross-correlation with a 0.2 s and 0.3 s time window for P and S waves, respectively. Event pairs with cross-correlation coefficient higher than 0.7 (at 4–50 Hz) were retained for relative relocation through GrowClust (Trugman and Shearer, 2017). The final relocated catalog includes a total of 29,669 earthquakes spanning over the entire monitored region (Fig. 4c).

3.3. Waveform amplitude calibration

To ensure consistent magnitude calibration across the four types of instruments, which may have different amplitude responses, we designed a "4In1" site where all devices were buried in a shared tray (Fig. 2). We estimated the waveform amplitude ratios among four seismographs using the sliding-window cross-correlation (SCC) method (Yang et al., 2009). Before performing three-component cross-correlation, we removed instrument responses and then applied a highpass filter of 5 Hz to recorded events (Fig. 5a). We accepted amplitude ratios with a cross-correlation coefficient greater than 0.7, yielding 525 qualified events. Among the four devices, TVG-63 records the largest amplitude (Fig. 5a). Taking HR3C as a reference for amplitude ratio estimation, statistical median values of amplitude ratios for TVG-63, EPS-2-M6Q, and QS-05A are 4.0, 1.8, and 2.2, respectively (Fig. 5b). Since all four devices were deployed in a ~ 1.2 m tray in the same manner (Fig. 2b), we infer that the variations are mainly due to device differences. We then applied amplitude corrections based on the estimated median coefficients to all stations before magnitude calibration.

3.4. Magnitude calibration

The local magnitude of the relocated catalog is calculated based on S-wave amplitude energy by the following equation:

$$M_L = \log_{10}A + 2.56\log_{10}D + C \tag{1}$$

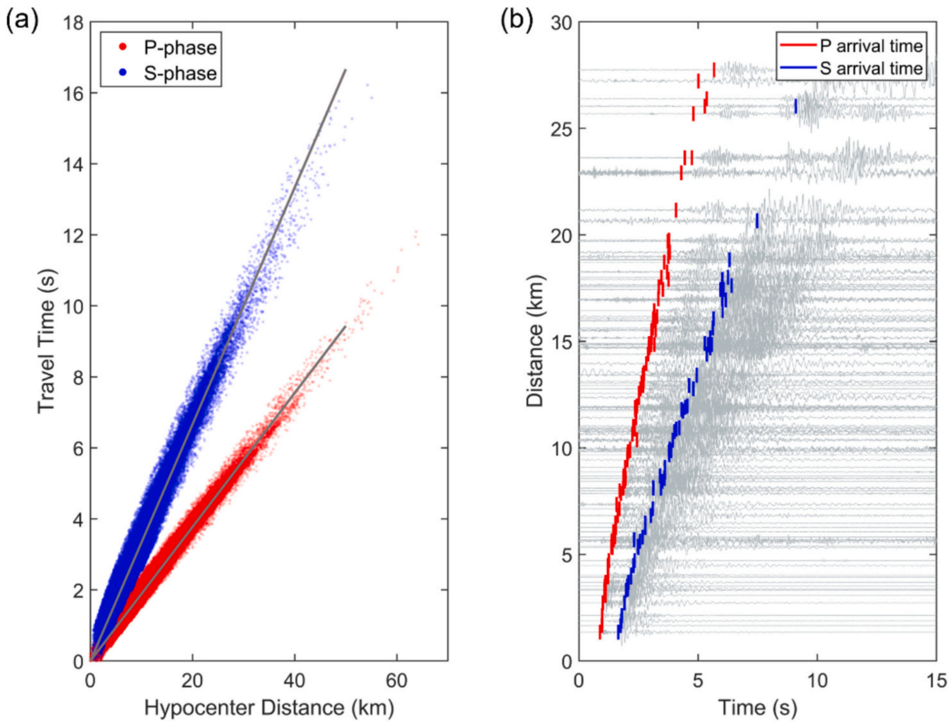

Fig. 3. Event association using REAL. (a) Travel time versus hypocenter distance plot of 42,497 associated events. Straight black lines indicate the fitted approximate velocities of P wave (5.3 km/s) and S wave (3.0 km/s). (b) An example earthquake (M_L 1.46) associated via REAL with P (red lines) and S (blue lines) arrival times picked by PhaseNet. Only vertical component waveforms (filtered from 2 to 30 Hz) are shown here. (For interpretation of the references to colour in this figure legend, the reader is referred to the web version of this article.)

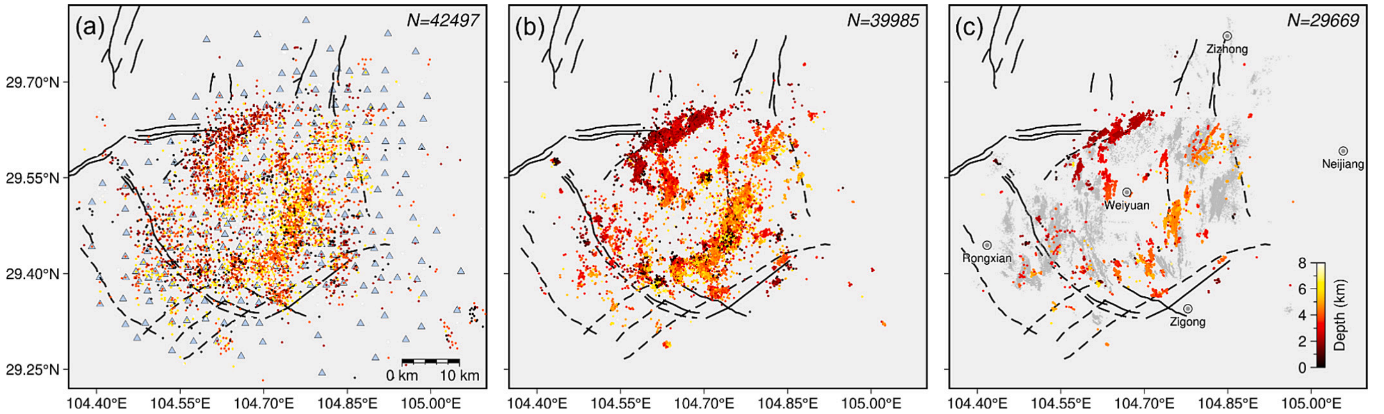

Fig. 4. Map view of seismicity at each of the sequential location steps during LOC-FLOW: (a) REAL; (b) HypoInverse; (c) GrowClust. The triangles show the seismic stations. The gray dots are events during 2015–2016 (Sheng et al., 2022) and 2019–2021 (Zi et al., 2023), respectively. (For interpretation of the references to colour in this figure legend, the reader is referred to the web version of this article.)

After removing the instrument response and calibrating waveform amplitudes, the waveforms were convolved with the response of a Wood-Anderson seismometer. The amplitude A is defined as the maximum square root sum of the three channels within a window starting 0.5 s before the P-wave arrival and ending 3 s after the S-wave arrival. We calibrated the constant C as −1.09 based on the magnitudes of 10 $M_L \geq 2.5$ events in the EarthX catalog (Table S1). The final M_L of each earthquake was calculated as the median value of M_L estimates from individual stations.

The magnitude of completeness (M_c) is estimated by the maximum curvature method (Wiemer, 2001). The *b* value of the Gutenberg-Richter (G-R) law (Gutenberg and Richter, 1944) is calculated via the maximum-likelihood estimation method (Bender, 1983). Since the maximum curvature method may underestimate the M_c value, we added a correction term of 0.2 when estimating *b* value. The standard error of *b* value is estimated following Shi and Bolt (1982). After magnitude calibration, the detected earthquakes are concentrated between M_L −1.35 and M_L 3.42, with a completeness magnitude M_c of −0.24 (Fig. S2).

4. Results

Finally, we detected 42,497 earthquakes, among which 29,669 events were relocated using cross-correlation differential times. To evaluate the location uncertainties of these relocated events, we applied a bootstrapping analysis to estimate their relative location uncertainties, resulting in median values of 34 m for epicenters and 38 m for depth. Overall, 90 % of the relocated events have uncertainties less than 120 m for epicenters and 150 m for depths (Fig. S3). These uncertainties are

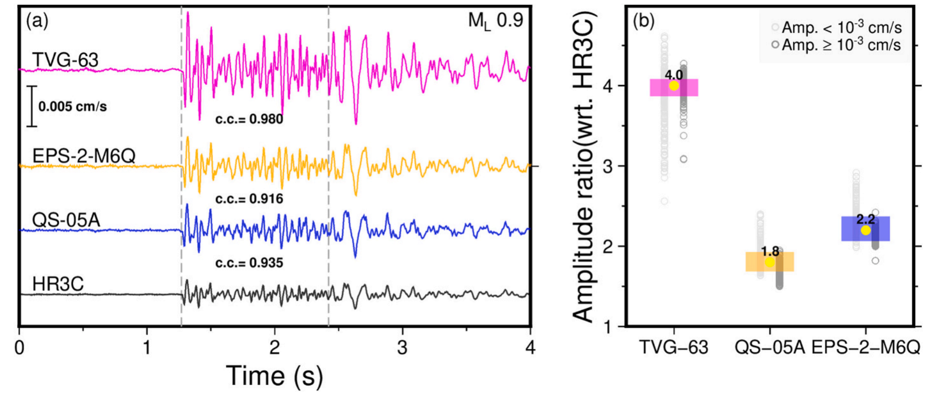

Fig. 5. Example waveforms from the "4In1" site. (a) *Z*-component velocities recorded at the four stations for an M_L 0.9 earthquake (c.c.: cross-correlation coefficient). The dashed lines represent the P- and S-wave arrival times. (b) Event amplitude ratios with reference to (wrt.) the HR3C recordings (circles), 25–75 % range (bars), and median values (yellow dots). Events with maximum amplitudes lower and higher than 10^{-3} cm/s are shown in light and dark gray, respectively. (For interpretation of the references to colour in this figure legend, the reader is referred to the web version of this article.)

comparable to other induced seismicity studies, which show relative uncertainties within a hundred-meter scale (Igonin et al., 2021; Zhang et al., 2024b; Glasgow et al., 2021; Tan et al., 2020).

Seismicity in the WSGF during the study period exhibited significant variability across different regions and time intervals. Compared to previously published catalogs (Sheng et al., 2022; Zi et al., 2023), our catalog shows a relatively lower level of seismic activity in the western part of WSGF. Based on spatial distributions, our catalog reveals five primary seismic clusters (R1-R5; Fig. 6), among which R1, R2, and R3 are newly emerged and appear to be especially associated with recent HF wells. In contrast, R4 and R5 have been active since at least 2019 (Li et al., 2024; Zi et al., 2023) and are closely located to mapped faults (Fig. 4c and S4a). The earthquakes exhibit distinct linear patterns primarily aligned NE-SW and NW-SE (Fig. 6a), consistent with those

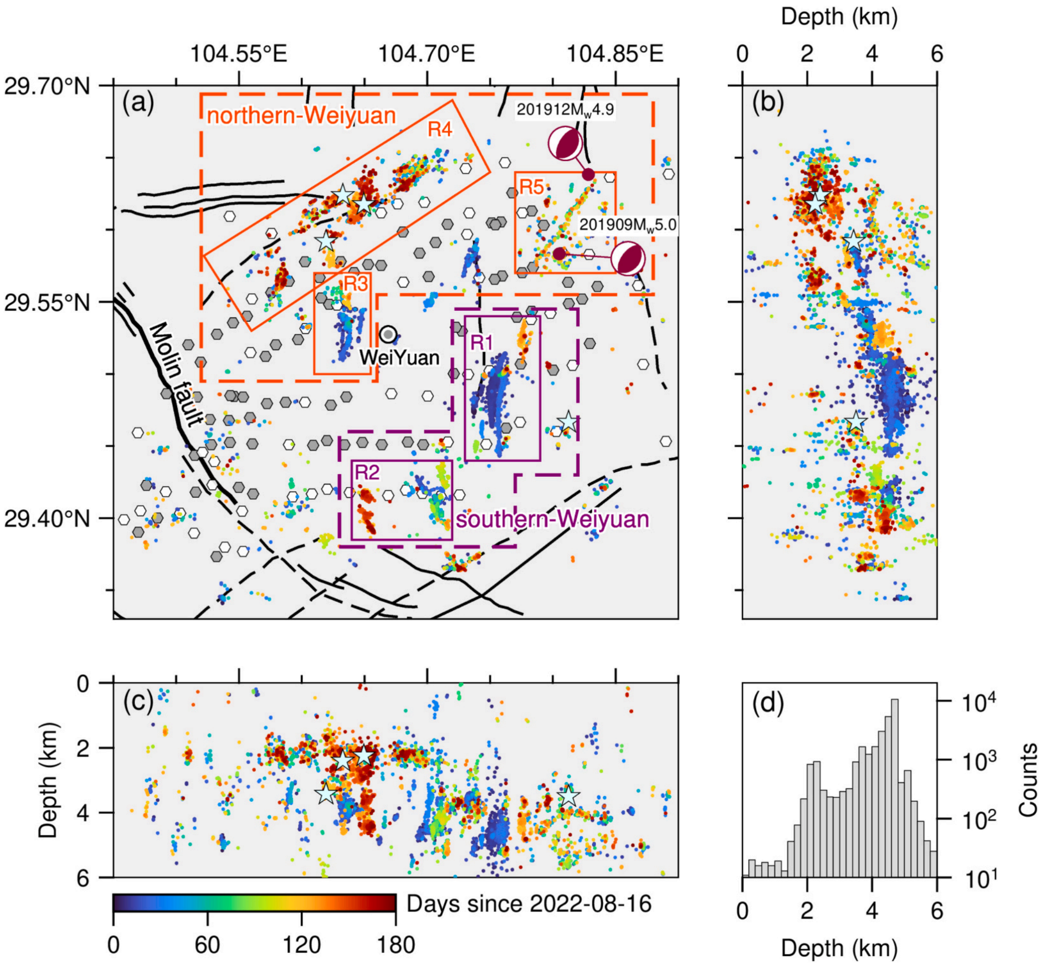

Fig. 6. The distribution of relocated seismicity in the WSGF. (a) Map view with regions and clusters (R1-R5) as labeled. The light cyan stars represent four $M_L > 3$ events in our catalog. (b) Projection of relocated seismicity along latitude. (c) Projection of relocated seismicity along longitude. (d) Counts of earthquakes over depths. (For interpretation of the references to colour in this figure legend, the reader is referred to the web version of this article.)

observed in previous catalogs. The events have shallow hypocentral depths (< 6 km), which vary between clusters and exhibit two prominent peaks at approximately 2 km and 4.5 km (Fig. 6d). Near the Weiyuan anticline, seismicity is concentrated at depths of ~2 km, whereas in the southern part of Weiyuan, earthquakes are generally deeper, averaging ~5 km (Fig. 6b). Compared to previous catalogs, the average event depths in our catalog are generally deeper (Fig. S4b). This is primarily attributed to the R1 cluster, where earthquakes are densely concentrated at depths around 4–5 km.

For elaboration, we separate earthquakes into northern and southern Weiyuan seismicity and introduce their characteristics, respectively. This classification is mainly based on the weak seismicity in the western part and the significant depth difference between the northern and southern regions.

4.1. Southern-Weiyuan seismicity

Seismicity in the southern-Weiyuan is notably active, including 21,943 events, accounting for 74 % of the total catalog. However, only one $M_L > 3$ event occurred during our study period, histograms of earthquakes show a clear cutoff of magnitude at M_L 2.2, above which earthquake quantities are few, suggesting the limited fracture size in this area as it experienced limited structural deformation (Zi et al., 2023; Li et al., 2024). Spatially, events are concentrated near injection wells without apparent association with any known faults. The hypocentral depths predominantly range from 3 to 5 km, remaining above the Precambrian basement. The southern-Weiyuan block features several linearly distributed swarms, and we divided them into two clusters according to their fault strikes (R1 and R2; Fig. 6a).

The R1 cluster accounts for over 50 % of the total events (i.e., 17,661) with a minimum magnitude of −1.3. The best-fitting b value for this cluster is 1.3 ± 0.02 (Fig. 7a), indicating a relatively high proportion of small-magnitude events. Based on the occurrence time, seismicity within R1 is mainly active between August 16 – September 20, 2022 (stage I), and December 1–30, 2022 (stage II, Fig. 7b). The R1 cluster depicts several spatially distinct linear structures oriented in NE-SW and N-S directions. Cross-sectional profiles of R1 indicate a clear layered distribution of seismicity, with most events occurring at a depth of about 1 km below the Wufeng formation (Fig. 8).

As earthquakes in the R1 cluster outline several subparallel linear features (hereafter referred to as "sub-faults" for descriptive convenience), we examine the spatiotemporal evolution along the latitudinal direction (Fig. 9). Note that the term "sub-faults" used here does not necessarily imply the presence of pre-existing tectonic faults but rather refers to linear clusters whose physical origins may include fault or fracture reactivation, hydraulic stimulation, or other processes. During stage I, seismicity on different sub-faults overlapped in time. The earthquakes started on sub-faults F1, F2, and F5 at the beginning of the deployment (August 16, 2022; Fig. 9b). Subsequently, repeated earthquakes were observed on the sub-faults F2-F5. Notably, seismic ruptures along the sub-fault F3 exhibited a stable recurrence interval of about 24 h (Fig. 9c). Toward the end of stage I, earthquakes mainly concentrated on sub-faults F5 and F6. In stage II, earthquakes mainly occurred along sub-fault F7, showing a clearly diffusion-like earthquake migration (Fig. 9e). For sub-faults F1 and F7, the migration fronts can be modeled as fluid diffusion processes, with best-fitting hydraulic diffusivities of 0.07 and 0.02 m^2/s, respectively (Figs. 9d, e).

The R2 cluster consists of multiple distinct sub-faults that are subparallel and oriented in the NW direction (Fig. 10a). Earthquake depths range from 3 km to 5 km, with most events occurring below the Wufeng formation, except for those near L9, which are situated above the Wufeng formation (Fig. 10d). The best-fitting b value for R2 cluster is 0.89 ± 0.02. The R2 cluster exhibits a distinct monthly periodicity (Fig. 7d) and the hydraulic diffusivities for individual swarms range from 0.008 m^2/s to 0.16 m^2/s (Fig. 11).

4.2. Northern-Weiyuan seismicity

Compared to the southern-Weiyuan block, seismicity in the northern-Weiyuan block is shallower and less active. However, more events with relatively larger magnitudes took place, including three $M_L > 3.0$ events (Fig. 6). According to the spatial and temporal characteristics of seismicity, we divided them into three clusters (R3-R5; Fig. 6a).

The R3 cluster exhibits a NE-striking fault system (Fig. 12a). Along the profiles, the event depths gradually increase from north to south (Figs. 12b, c). Similar to R1 and R2, seismicity in R3 is spatially correlated with injection wells. For sub-faults that can be distinguished from others (i.e., F1-F3 in Fig. 12a), the hydraulic diffusivities range from

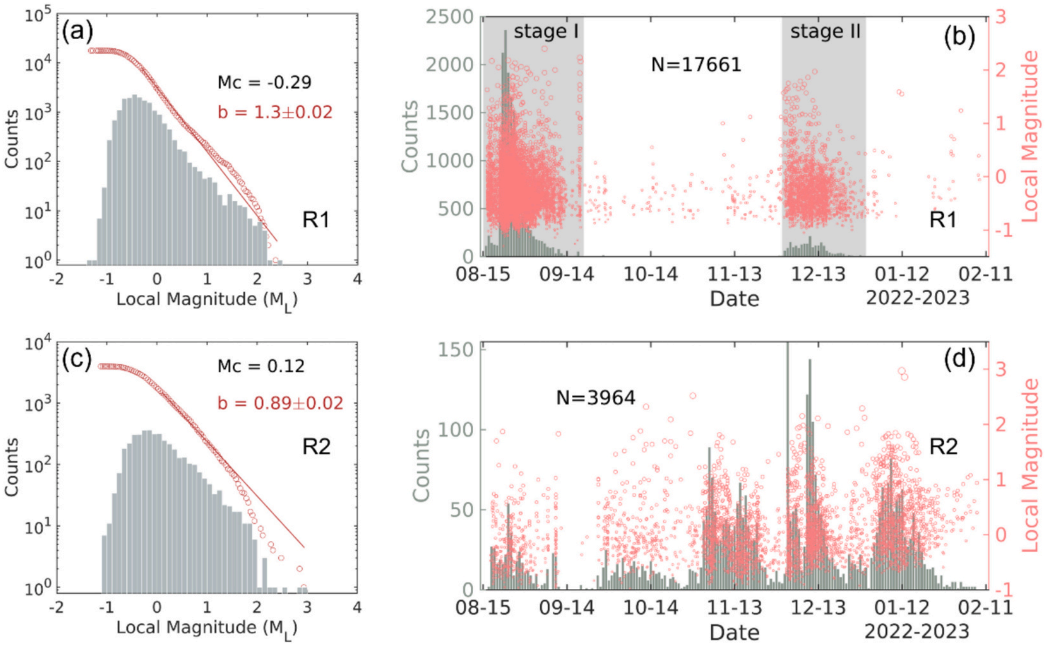

Fig. 7. (a) and (c) are frequency-magnitude distributions for R1 and R2 clusters, respectively. The red line represents the maximum likelihood fit for the Gutenberg-Richter relation. (b) and (d) are event rates over date for the R1 and R2 clusters, respectively. The gray bars at the bottom are the count of earthquakes each day.

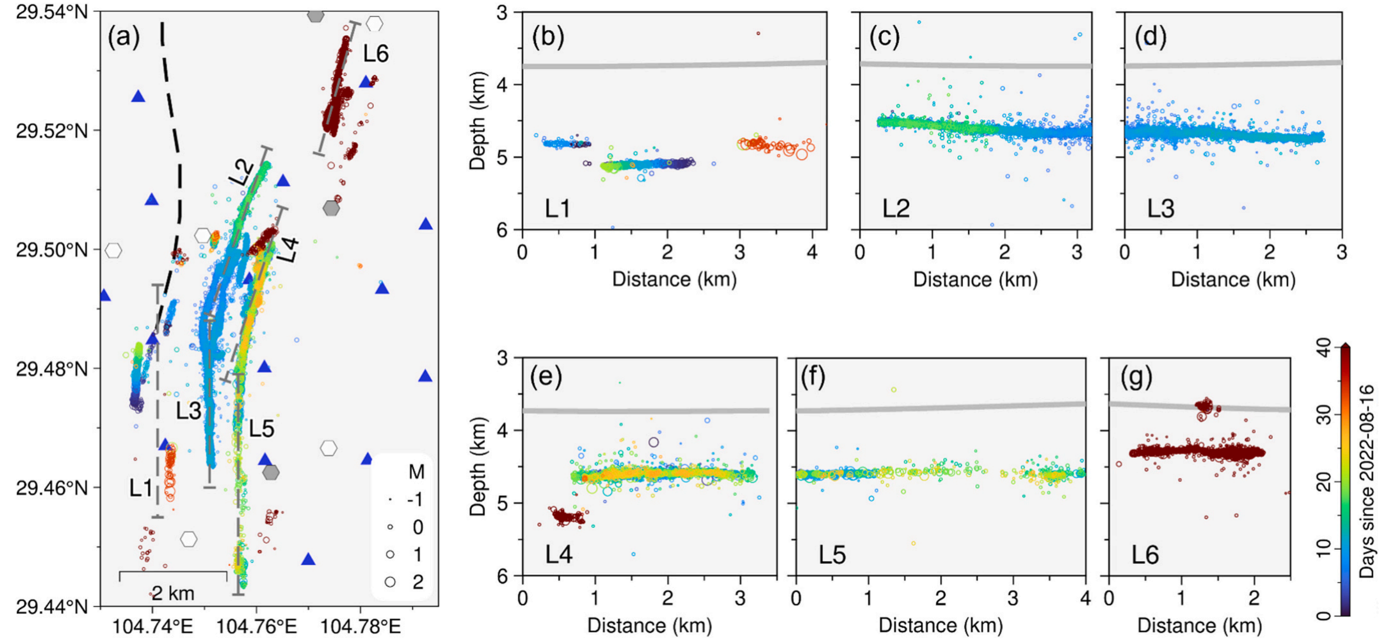

Fig. 8. Spatial-temporal distribution of earthquakes in R1 cluster of the southern-Weiyuan block (a) and the projections of seismicity along the lines L1-L6 at depth (b)-(g).

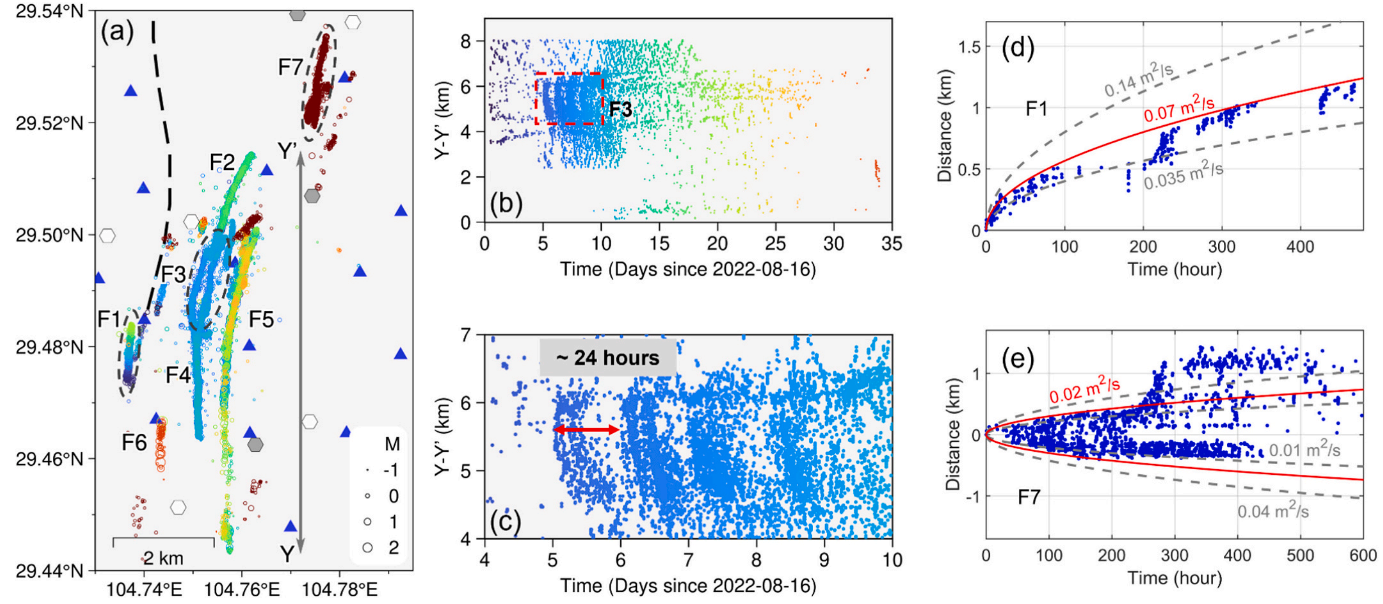

Fig. 9. Time-projection along the cross-sections Y-Y′ and the spatial-temporal migration rates for sub-faults in R1 cluster. (a) Seven identified sub-faults F1-F7 within the R1 cluster. (b) Time-projection along Y-Y′. (c) Zoom-in of the red box region in (b). (d)-(e) The spatial and temporal migration rates for the seismicity in sub-faults F1 and F7. The gray dashed lines are double and half of the hydraulic diffusivities. (For interpretation of the references to colour in this figure legend, the reader is referred to the web version of this article.)

$0.006\ m^2/s$ to $0.04\ m^2/s$ (Fig. 13). The R4 cluster is closely associated with faults revealed by previous 3D seismic exploration. In the northern section, the apparent 15 km-long fault can be segmented into three sections (represented by profile lines of L13-L15; Fig. 14a), with seismicity primarily located at ~3 km depths, marking the shallowest clusters in our study. Despite a relatively low seismicity rate, R4 hosts three out of four $M_L > 3$ earthquakes of our detection.

For seismicity within the R5 cluster, the spatial distribution reveals an ~8 km NE-SW fault consistent with that previously identified for the 2019 M_w 5.0 event (Figs. 15a, b; Zi et al., 2025). The west-dipping depth distribution further suggests that these events are aftershocks of the M_w 5.0 earthquake. The best-fitting b value for R3, R4, and R5 clusters are 0.94 ± 0.03, 0.63 ± 0.02, and 0.86 ± 0.06, with R4 exhibiting the lowest b value in the WSGF (Fig. S5).

5. Discussion

5.1. Spatial distribution and migration patterns of relocated seismicity

In this study, the spatial distribution and migration patterns of seismicity in the WSGF reveal the complex interactions between HF processes, pre-existing fault structures, and subsurface fluid migration.

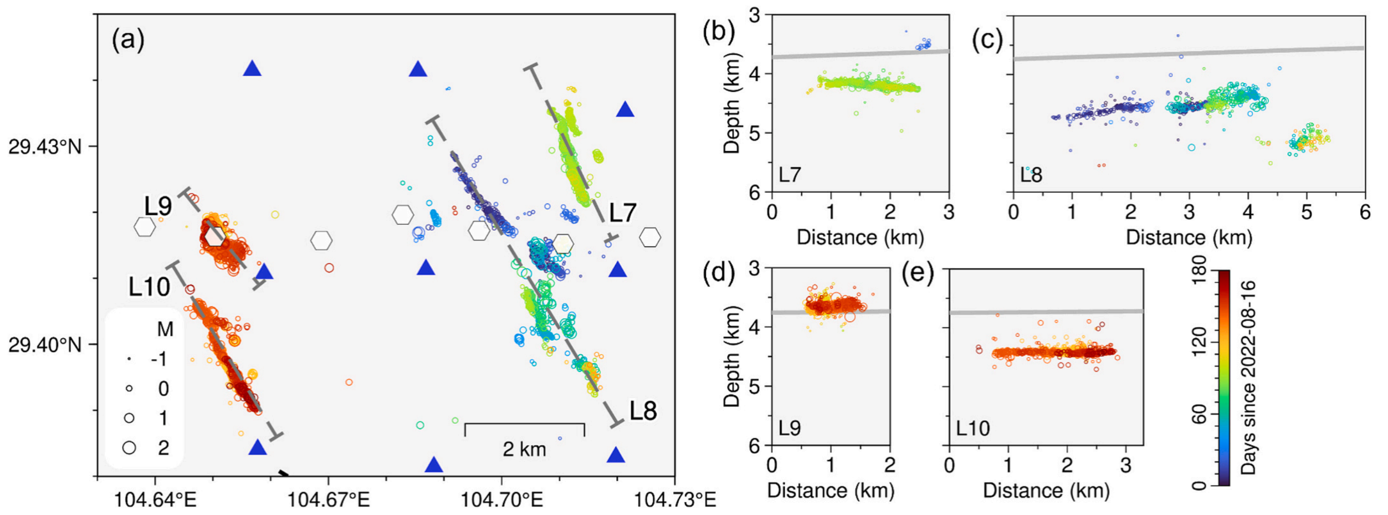

Fig. 10. (a) Spatial-temporal distribution of earthquakes in R2 cluster of southern-Weiyuan block. (b)-(e) The projections of seismicity along the lines (L7-L10) along depth.

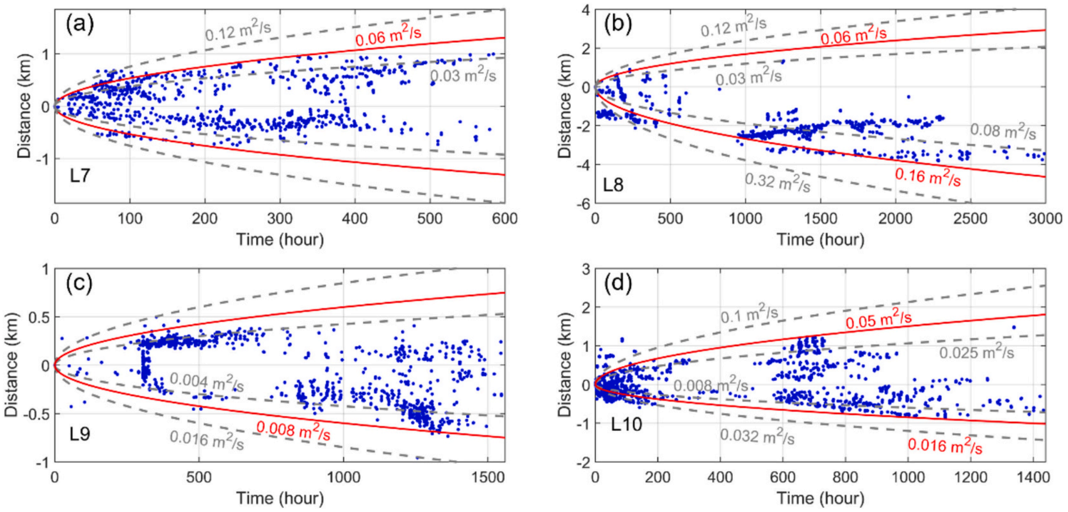

Fig. 11. Spatial and temporal migration rates for the seismicity in R2 cluster along L7–L10 (see Fig. 10). The red solid lines show the theoretical propagating pore pressure front, and the numbers indicate the hydraulic diffusivities. The gray dashed lines are double and half of the hydraulic diffusivities. (For interpretation of the references to colour in this figure legend, the reader is referred to the web version of this article.)

Horizontally, the newly recognized earthquake clusters R1-R3 are closely associated with HF wells, revealing the activation of latent faults and/or fractures (Fig. 6). The predominant NE and NW strikes of these clusters align with the expected orientations of conjugate shear fractures under oblique compression (Zhang et al., 2023). Depth-wise, seismicity deepens from north to south, corresponding to the increasing depth of the target shale layer (i.e., the Wufeng-Longmaxi formation) across the field (Ma et al., 2020). Furthermore, seismicity migration patterns provide indirect insight into fracturing operations in the WSGF region, where direct industrial activity data are unavailable. For example, the spatiotemporal evolution of clusters R1-R3 may reflect the monthly migration of HF operations.

Several distinct seismicity migration behaviors were observed with different temporal and spatial characteristics in the northern-Weiyuan and southern-Weiyuan blocks:

(1) R1-R3 clusters: The complex spatial-temporal distribution of seismicity in the R1 cluster is likely influenced by multiple injection wells. Pore-pressure diffusion through high-permeability pathways appears to be the dominant triggering mechanism for sub-faults F1 and F7, as evidenced by parabolic earthquake migration patterns. Notably, we observed repeated ruptures on sub-fault F3 within a confined area, implying the presence of a persistent fluid migration channel. The relatively stable time intervals (about 24 h; Fig. 9c) between ruptures on F3 indicate cyclic pressure release, likely controlled by HF operations. The high *b* value also indicates the characteristic of injection-induced seismicity on new faults and/or fractures, consistent with the lack of significant pre-existing faults in this region, suggested by previous studies (Zi et al., 2023; Li et al., 2024).

Similarly, the diffusion-like migration patterns observed in the R2 and R3 clusters also imply that these earthquakes are primarily driven by pore-pressure propagation. The spatially segmented sequences indicate pre-existing fractures reactivated sequentially by the injected fluids. We model earthquake migrations as fluid diffusion processes with hydraulic diffusivity ranging from 0.006 m^2/s to 0.16 m^2/s, generally close to the observations of Zi et al. (2025) but slower than the results of Sheng et al. (2022). This relatively broad range of hydraulic diffusivity values likely reflects several factors, including spatial

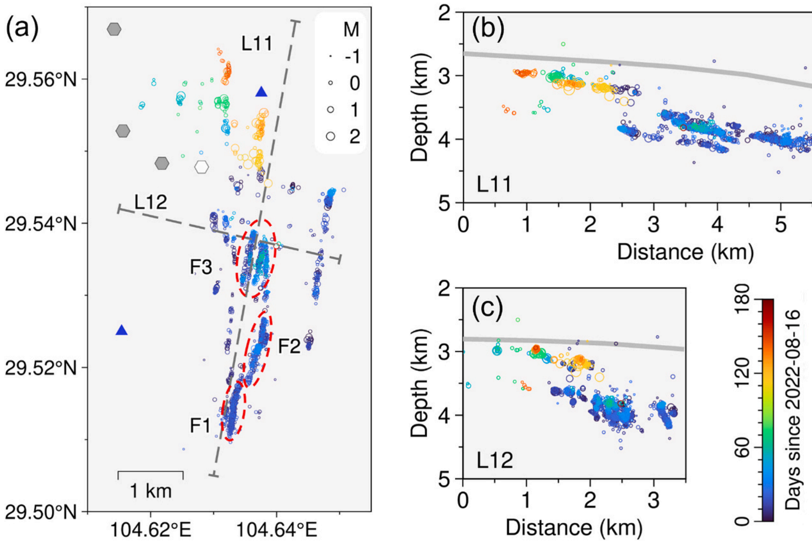

Fig. 12. (a) Spatial-temporal distribution of earthquakes in R3 cluster of northern-Weiyuan block. (b)-(c) The projections of seismicity along the lines (L11 and L12) at depth.

variations in permeability and porosity, differences in injection rates and volumes, and variability in fracture connectivity. Furthermore, in calculating hydraulic diffusivity, we did not explicitly distinguish between events potentially occurring near horizontal wells and those on faults, which may have caused the diffusivity estimates to be affected by the time intervals between hydraulic fracturing stages. However, we only modeled diffusion for clusters that exhibit clear parabolic migration patterns and excluded sequences with regular time intervals, minimizing such artifacts. Most events occurred along the modeled diffusion fronts with decent fitting (i.e., clear parabolic shape). Therefore, despite the unavailability of HF operational data, the results still offer meaningful constraints on fluid-driven processes, and we interpret pore-pressure diffusion as a plausible triggering mechanism for these clusters.

(2) R4 cluster: Unlike R1-R3, the R4 cluster is associated with a fault system imaged by previous 3D seismic exploration, spanning over a ∼ 15 km fault segmented into three zones (Fig. 14a). The seismicity in R4 shows no apparent diffusion-like migration pattern that would confirm direct fluid-triggered processes. Instead, the observed pre-mainshock–aftershock sequence suggests that tectonic stress accumulation along the segmented fault system could be the dominant mechanism (Fig. S5d). In this view, the segmentation likely leads to stress concentration at the boundaries between fault segments, which in turn facilitates episodic ruptures. The genesis of the R4 cluster appears more directly linked to inherent fault complexity and natural tectonic loading, rather than to fluid injection. Lastly, the low *b* value of R4 (i.e., 0.63 ± 0.02) indicates a higher seismic risk potential, necessitating continuous monitoring (Fig. S5c).

Most clustered earthquakes follow a diffusion distribution pattern, indicating these earthquakes are driven by pore-pressure diffusion (Figs. 9, 11, 13). Some outlier earthquakes that fall ahead of diffusion curves at initial stages were likely triggered by the poroelasticity effect due to nearby fracking operations. In recent years, field observations (e.g., Eyre et al., 2019), in-situ measurements (e.g., Guglielmi et al., 2015), and numerical simulations (Bhattacharya and Viesca, 2019; Jacquey and Viesca, 2023; Yang et al., 2023) emphasize the role of aseismic slip in inducing seismicity. Although theoretical migration patterns differ between pore-pressure diffusion and aseismic slip (Yang et al., 2023), discriminating between the two in field observations remains challenging due to structure heterogeneities and unknown underground stress conditions. It is likely that aseismic slip was involved in inducing some observed seismicity in this work.

5.2. *The long-lasting aftershocks of the 2019 M_w 5.0 event*

The September 2019 M_w 5.0 (M_L 5.6) earthquake marks the largest seismic event recorded to date in the WSGF. This event has been comprehensively investigated across multiple domains, including focal mechanism and centroid depth determination (Yi et al., 2020), rupture directivity analysis (Sheng et al., 2020), coseismic surface deformation mapping (Zhang et al., 2024a), fault identification through industrial seismic reflection profiles (Liu et al., 2023a), high-resolution earthquake relocation using near-fault observations, as well as numerical simulations of triggering physics (Zi et al., 2025). These multidisciplinary studies converge on three key characteristics:

(1) The reverse-faulting earthquake ruptured a northeast-striking fault (strike 40°, dip 39°) at a hypocenter depth of 4.7 km and a centroid depth of 4.5 km;
(2) The rupture area covered approximately 11 km^2, with intense aftershock activity concentrated along its periphery;
(3) The fault exhibited 11 months precursory activation driven by post-injection aseismic slip.

Notably, during our six-month monitoring campaign from August 2022 to February 2023 (three years post-event), we detected persistent seismicity within the source region (Fig. 15a). These earthquakes spatially coincide with immediate aftershock locations, delineating the fault plane and enveloping the elliptical rupture area (Figs. 15b, c), indicating their nature as protracted aftershocks. A notable offset exists between the aftershock distributions mapped by Zi et al. (2025) and our study (dashed v.s. solid ellipses in Fig. 15b). Such a discrepancy could be attributable to differences in velocity models: Zi et al. (2025) employed 1D borehole-derived velocity models with apparent low-velocity layers, whereas our study utilized simplified 1D velocity models from the WSGF-wide tomography (Zi et al., 2023), providing broader regional representation. Compared to the borehole-derived model, the relatively higher P-wave and S-wave velocities in the shallow layers (i.e., 0–3.5 km; Fig. S6) of our model could result in deeper hypocenters.

The prolonged aftershock sequence (magnitude up to M_L 2.0) suggests persistent fault stress heterogeneity following the M_w 5.0

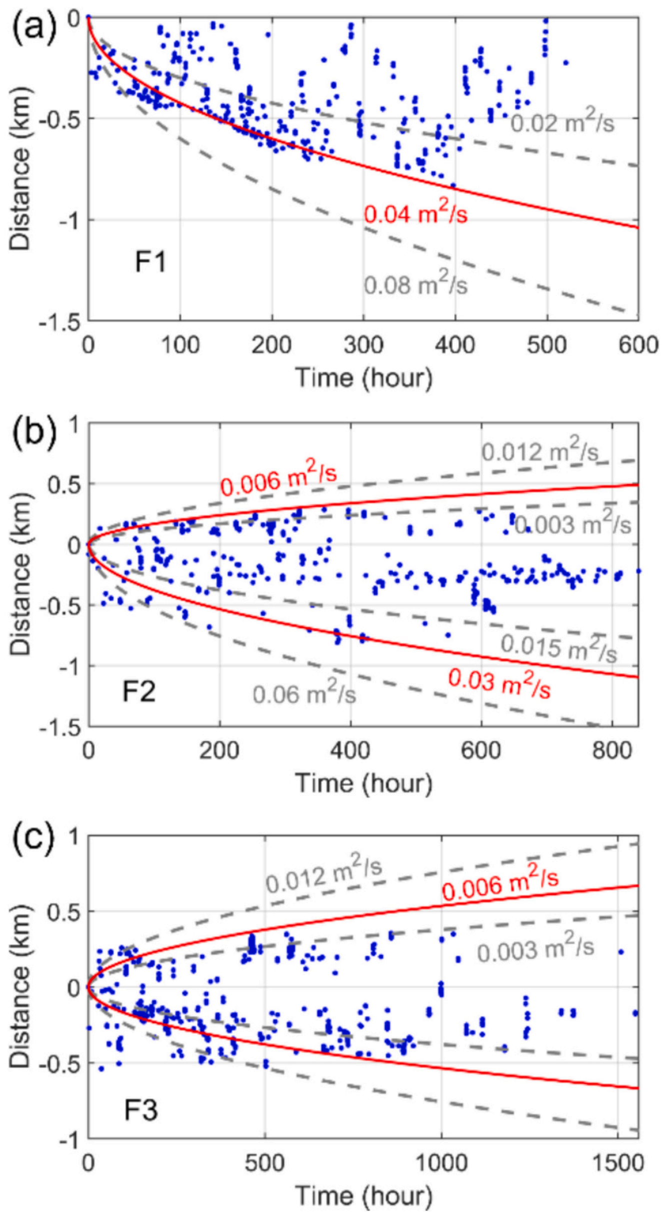

Fig. 13. Spatial and temporal migration rates for the sub-faults F1-F3 in R3 cluster. The red solid lines show the theoretical propagating pore pressure front, and the numbers indicate the hydraulic diffusivities. The gray dashed lines are double and half of the hydraulic diffusivities. (For interpretation of the references to colour in this figure legend, the reader is referred to the web version of this article.)

earthquake. These observations underscore the importance of long-term seismic monitoring in regions with induced or triggered seismicity. The sustained aftershock activity following the M_w 5.0 event highlights the need to account for delayed hazards in post-seismic risk assessments, particularly in industrial settings such as shale gas fields.

On the contrary, we observed no aftershocks of the December 2019 M_w 4.9 event, the second largest triggered event in the WSGF, which occurred three months after the M_w 5.0 earthquake. It is intriguing that the two adjacent moderate-size events pose a stark contrast in aftershock productivity as they have similar focal mechanisms and focal depths with the M_w 4.9 event slightly shallower (Yi et al., 2020). A plausible explanation is that residual stress heterogeneity from the M_w 5.0 earthquake sustained its aftershock activity, while the M_w 4.9 event lacked such driving conditions. Unfortunately, the lack of high-resolution seismic catalogs during the M_w 4.9 event's occurrence period hinders further investigation into the contrasting seismogenic conditions.

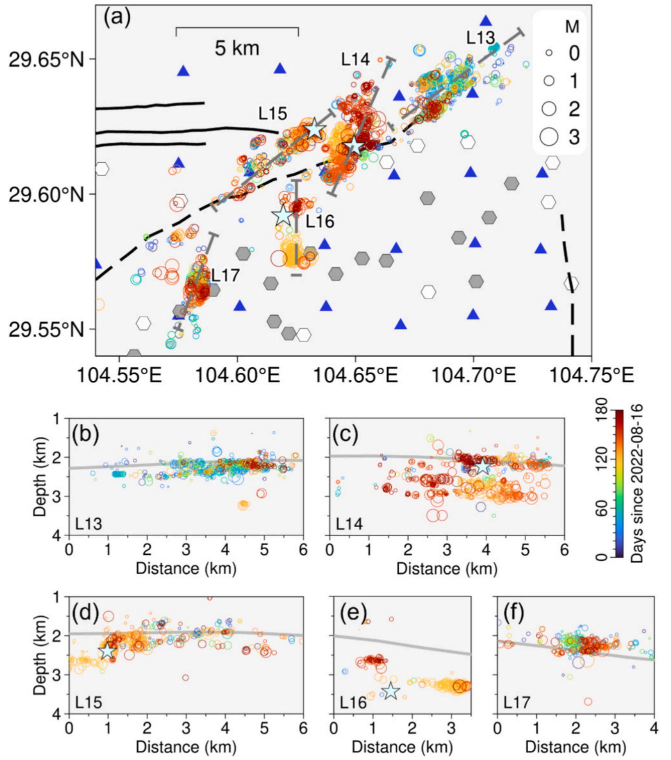

Fig. 14. (a) Spatial-temporal distribution of earthquakes in R4 cluster of northern-Weiyuan block. (b)-(f) The projections of seismicity along the lines (L13-L17) at depth. The light cyan stars represent $M_L > 3$ events. (For interpretation of the references to colour in this figure legend, the reader is referred to the web version of this article.)

6. Conclusion

In this study, we deployed a dense seismic array consisting of four types of seismometers in the WSGF for monitoring induced seismicity and constructing a high-resolution earthquake catalog. Waveform cross-correlation analysis at the “4In1” site revealed significant waveform amplitude variation among different seismometer types, underscoring the necessity for waveform consistency assessment in nodal arrays incorporating diverse instruments.

We finally relocated 29,669 earthquakes through LOC-FLOW, with the M_c of -0.24. The spatial and temporal distribution of seismicity revealed distinct clustering patterns: In the southern-Weiyuan block, all clusters were newly emerged and closely associated with HF wells. The migration patterns of selected seismic swarms, exhibiting clear parabolic features, indicated pore-pressure diffusion as the potential triggering mechanism. The estimated hydraulic diffusivities ranged from 0.006 m^2/s to 0.16 m^2/s, falling within a reasonable range and capturing most events along the modeled diffusion front (Dai et al., 2024; Zi et al., 2025). In contrast, most seismicity in the northern-Weiyuan block occurred along pre-existing faults, suggesting the combination of fluid-induced and stress-driven mechanisms in the WSGF. Additionally, we observed persistent aftershocks (i.e., over three years) near the 2019 M_w 5.0 rupture zone; such delayed seismic responses should be considered in hazard assessment and risk mitigation strategies for shale gas production regions.

Overall, our study presents preliminary results based on the newly acquired dataset in the WSGF, providing a robust catalog and a preliminary overview of key seismic clusters. These findings emphasize the

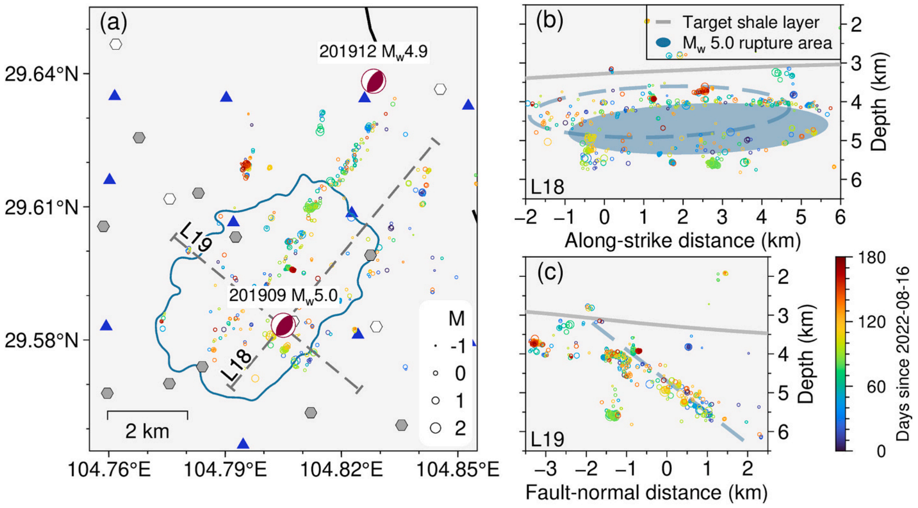

Fig. 15. (a) Spatial-temporal distribution of earthquakes around the 2019 M_w 5.0 earthquake in R5. The coseismic surface deformation zone is outlined by jade-blue. (b) Along-strike section plot of seismicity (L18). The light gray line stands for the target shale layer. The jade-blue dashed ellipse represents the outline of the rupture area constrained by earthquake relocations from the velocity models of Zi et al. (2025). The solid ellipse stands for the region encompassed by earthquakes relocated using velocity models in this study. (c) Fault-normal section plot of seismicity (L19). The dashed jade-blue line represents the accounting fault of the M_w 5.0 event. (For interpretation of the references to colour in this figure legend, the reader is referred to the web version of this article.)

value of dense seismic monitoring for capturing the spatiotemporal complexity of induced seismicity. While several clusters (e.g., R1-R3) are spatially correlated with HF platforms, we reserve definitive causal interpretations due to the current lack of detailed HF operational information. Nonetheless, the results establish a solid foundation for future research of induced seismicity and highlight the need for continued monitoring and adaptive risk mitigation strategies in active shale gas fields.

CRediT authorship contribution statement

Lichun Yang: Writing – review & editing, Writing – original draft, Visualization, Methodology, Investigation, Formal analysis. **Jinping Zi:** Writing – review & editing, Writing – original draft, Visualization, Methodology, Formal analysis. **Ruijia Wang:** Writing – review & editing, Supervision, Project administration, Investigation, Funding acquisition, Conceptualization. **Hongfeng Yang:** Writing – review & editing, Supervision, Project administration, Investigation, Funding acquisition, Conceptualization.

Declaration of competing interest

The authors declare that they have no known competing financial interests or personal relationships that could have appeared to influence the work reported in this paper.

Acknowledgment

We thank the enterprise TAIDE from Zhuhai, Guandong, China, for providing 50 seismometers during the fieldwork. Acknowledgment is delivered to colleagues from the Sichuan Earthquake Agency, Southern University of Science and Technology, and The Chinese University of Hong Kong for the fieldwork. This work is supported by the National Natural Science Foundation of China (No. U2139203 and No. 42374068) and Shenzhen Key Laboratory of Deep Offshore Oil and Gas Exploration Technology (No. ZDSYS20190902093007855). R.W. is also supported by the Shenzhen Fundamental Research Program (No. 202208142135190001), and the Leading Talents Program of Guangdong Province (No. 2021QN02G113). H. Y. is also supported by the Research Grants Council, University Grants Committee, Hong Kong (No. 14303721 and No. 14306122), and the Faculty of Science at The Chinese University of Hong Kong.

Appendix A. Supplementary data

Supplementary data to this article can be found online at https://doi.org/10.1016/j.tecto.2025.230862.

Data availability

Reported earthquakes of M ≥ 4 events between 2009 and 2024 were downloaded from the China Earthquake Data Center (https://data.earthquake.cn). EarthX catalog can be downloaded from https://bafangseis.com/cn/earthquakes.html. Figures are prepared using GMT (Wessel et al., 2019) and Matlab.

References

Bender, B., 1983. Maximum likelihood estimation of b values for magnitude grouped data. Bull. Seismol. Soc. Am. 73, 831–851. https://doi.org/10.1785/bssa0730030831.

Bhattacharya, P., Viesca, R.C., 2019. Fluid-induced aseismic fault slip outpaces pore-fluid migration. Science 364, 464–468. https://doi.org/10.1126/science.aaw7354.

Chen, H., Meng, X., Niu, F., Tang, Y., Yin, C., Wu, F., 2018. Microseismic monitoring of stimulating shale gas reservoir in SW China: 2. Spatial clustering controlled by the preexisting faults and fractures. J. Geophys. Res. Solid Earth 123, 1659–1672. https://doi.org/10.1002/2017JB014491.

Chu, R., Sheng, M., 2023. Stress features inferred from induced earthquakes in the Weiyuan shale gas block in southwestern China. J. Geophys. Res. Solid Earth 128. https://doi.org/10.1029/2022JB025344 e2022JB025344.

Dai, J., Liu, J., Liu, C., Yang, J., Xue, F., Tang, Y., Liu, J., Liu, D., Dai, S., 2024. Regional characteristics of seismicity associated with hydraulic fracturing in the Southern Sichuan Basin of China. Rock Mech. Rock. Eng. 57, 6971–6996. https://doi.org/10.1007/s00603-024-03891-w.

Du, G., Wu, Q., Zhang, X., Zhang, R., 2021. Activity characteristics of moderate and small earthquakes and fine crustal feature beneath Weiyuan, Sichuan and adjacent areas. Chin. J. Geophys. (in Chinese) 64, 3983–3996. https://doi.org/10.6038/cjg2021O0452.

Eaton, D.W., Igonin, N., Poulin, A., Weir, R., Zhang, H., Pellegrino, S., Rodriguez, G., 2018. Induced seismicity characterization during hydraulic-fracture monitoring with a shallow-wellbore geophone array and broadband sensors. Seismol. Res. Lett. 89, 1641–1651. https://doi.org/10.1785/0220180055.

Ellsworth, W.L., 2013. Injection-induced earthquakes. Science 341, 1225942. https://doi.org/10.1126/science.1225942.

Eyre, T.S., Eaton, D.W., Garagash, D.I., Zecevic, M., Venieri, M., Weir, R., Lawton, D.C., 2019. The role of aseismic slip in hydraulic fracturing–induced seismicity. Sci. Adv. 5, eaav7172. https://doi.org/10.1126/sciadv.aav7172.

Feng, T., Wang, R., Fang, L., Wu, J., Yang, T., 2024. Microseismic constraints on the mechanical state of the Anninghe-Daliangshan fault zone, southeastern Tibetan

Plateau. Earth Planet. Sci. Lett. 639, 118765. https://doi.org/10.1016/j.epsl.2024.118765.

Glasgow, M., Schmandt, B., Wang, R., Zhang, M., Bilek, S.L., Kiser, E., 2021. Raton Basin induced seismicity is hosted by networks of short basement faults and mimics tectonic earthquake statistics. J. Geophys. Res. Solid Earth 126. https://doi.org/10.1029/2021JB022839 e2021JB022839.

Gu, Y.J., Sun, W., Yu, T.-C., Wang, J., Wang, R., Li, T., Schultz, R., 2024. Peace river induced seismic monitoring (PRISM) nodal seismic array. Seismol. Res. Lett. 96, 562–575. https://doi.org/10.1785/0220240029.

Guglielmi, Y., Cappa, F., Avouac, J.-P., Henry, P., Elsworth, D., 2015. Seismicity triggered by fluid injection–induced aseismic slip. Science 348, 1224–1226. https://doi.org/10.1126/science.aab0476.

Gutenberg, B., Richter, C.F., 1944. Frequency of earthquakes in California. Bull. Seismol. Soc. Am. 34, 185–188. https://doi.org/10.1785/BSSA0340040185.

Igonin, N., Verdon, J.P., Kendall, J.-M., Eaton, D.W., 2021. Large-scale fracture systems are permeable pathways for fault activation during hydraulic fracturing. J. Geophys. Res. Solid Earth 126. https://doi.org/10.1029/2020JB020311 e2020JB020311.

Jacquey, A.B., Viesca, R.C., 2023. Nucleation and arrest of fluid-induced aseismic slip. Geophys. Res. Lett. 50. https://doi.org/10.1029/2022GL101228 e2022GL101228.

Klein, F.W., 2002. User's guide to HYPOINVERSE-2000, a Fortran Program to Solve for Earthquake Locations and Magnitudes. In Open-File Report, 123.

Lei, X., Su, J., Wang, Z., 2020. Growing seismicity in the Sichuan Basin and its association with industrial activities. Sci. China Earth Sci. 63, 1633–1660. https://doi.org/10.1007/s11430-020-9646-x.

Li, J., Xu, J., Zhang, H., Yang, W., Tan, Y., Zhang, F., Meng, L., Zang, Y., Miao, S., Guo, C., Li, Z., Lu, R., Sun, J., 2023. High seismic velocity structures control moderate to strong induced earthquake behaviors by shale gas development. Commun. Earth Environ. 4, 188. https://doi.org/10.1038/s43247-023-00854-x.

Li, Y., Li, H., Huang, Y., 2024. Seismicity in the Weiyuan-Rongxian area, Sichuan basin, SW China. J. Asian Earth Sci. 272, 106241. https://doi.org/10.1016/j.jseaes.2024.106241.

Liu, G., Lu, R., He, D., Tao, W., Su, P., Zhang, W., Zhang, J., Xu, F., Sun, X., Wang, W., 2023a. Detailed imaging of a seismogenic fault that potentially induced the two 2019 weiyuan moderate earthquakes in the Sichuan Basin, China. Seismol. Res. Lett. 94, 1379–1391. https://doi.org/10.1785/0220220228.

Liu, Y., Yu, Z., Zhang, Z., Yao, H., Wang, W., Zhang, H., Fang, H., Fang, L., 2023b. The high-resolution community velocity model V2.0 of Southwest China, constructed by joint body and surface wave tomography of data recorded at temporary dense arrays. Sci. China Earth Sci. 66, 2368–2385. https://doi.org/10.1007/s11430-022-1161-7.

Liu, G., Lu, R., He, D., Tao, W., Huang, X., Su, P., Xu, F., Zhang, W., 2024. Cascade processes of induced and triggered earthquakes-Case study in the Weiyuan shale gas development area in Sichuan Basin, China. Tectonophysics 890, 230495. https://doi.org/10.1016/j.tecto.2024.230495.

Ma, X., Li, X., Liang, F., Wan, Y., Shi, Q., Wang, Y., Zhang, X., Che, M., Guo, W., Guo, W., 2020. Dominating factors on well productivity and development strategies optimization in Weiyuan shale gas play, Sichuan Basin, SW China. Pet. Explor. Dev. 47, 594–602. https://doi.org/10.1016/S1876-3804(20)60076-3.

Moein, M.J.A., Langenbruch, C., Schultz, R., Grigoli, F., Ellsworth, W.L., Wang, R., Rinaldi, A.P., Shapiro, S., 2023. The physical mechanisms of induced earthquakes. Nat. Rev. Earth Environ. 4, 847–863. https://doi.org/10.1038/s43017-023-00497-8.

Schultz, R., Skoumal, R.J., Brudzinski, M.R., Eaton, D., Baptie, B., Ellsworth, W., 2020. Hydraulic Fracturing-Induced Seismicity. Rev. Geophys. 58. https://doi.org/10.1029/2019RG000695 e2019RG000695.

Sheng, M., Chu, R., Ni, S., Wang, Y., Jiang, L., Yang, H., 2020. Source parameters of three moderate size earthquakes in Weiyuan, China, and their relations to shale gas hydraulic fracturing. J. Geophys. Res. Solid Earth 125. https://doi.org/10.1029/2020JB019932 e2020JB019932.

Sheng, M., Chu, R., Peng, Z., Wei, Z., Zeng, X., Wang, Q., Wang, Y., 2022. Earthquakes triggered by fluid diffusion and boosted by fault reactivation in Weiyuan, China due to hydraulic fracturing. J. Geophys. Res. Solid Earth 127. https://doi.org/10.1029/2021JB022963 e2021JB022963.

Shi, Y., Bolt, B.A., 1982. The standard error of the magnitude-frequency b value. Bull. Seismol. Soc. Am. 72, 1677–1687. https://doi.org/10.1785/bssa0720051677.

Tan, Y., Hu, J., Zhang, H., Chen, Y., Qian, J., Wang, Q., Zha, H., Tang, P., Nie, Z., 2020. Hydraulic fracturing induced seismicity in the Southern Sichuan basin due to fluid diffusion inferred from seismic and injection data analysis. Geophys. Res. Lett. 47. https://doi.org/10.1029/2019GL084885 e2019GL084885.

Tan, Y., Qian, J., Hu, J., Zhang, H., Xing, H., Li, J., Xu, J., Yang, W., Gu, N., Miao, S., 2023. Tomographic evidences for hydraulic fracturing induced seismicity in the Changning shale gas field, southern Sichuan Basin, China. Earth Planet. Sci. Lett. 605, 118021. https://doi.org/10.1016/j.epsl.2023.118021.

Tian, W., Wu, Q., Dai, K., Guo, R., Yao, Z., Qiang, Z., Deng, F., 2024. Seismological evidence for the existence of long-distance hydrological channel and its implication for fluid overpressure in Southern Sichuan, China. Geophys. Res. Lett. 51. https://doi.org/10.1029/2023GL107167 e2023GL107167.

Trugman, D.T., Shearer, P.M., 2017. GrowClust: a hierarchical clustering algorithm for relative earthquake relocation, with application to the Spanish Springs and Sheldon, Nevada, earthquake sequences. Seismol. Res. Lett. 88, 379–391. https://doi.org/10.1785/0220160188.

Wang, R., Schmandt, B., Zhang, M., Glasgow, M., Kiser, E., Rysanek, S., Stairs, R., 2020. Injection-induced earthquakes on complex fault zones of the Raton Basin illuminated by machine-learning phase picker and dense nodal array. Geophys. Res. Lett. 47. https://doi.org/10.1029/2020GL088168 e2020GL088168.

Wang, R., Yang, D., Chen, Y., Ren, C., 2023. Lighting up a 1 km fault near a hydraulic fracturing well using a machine learning-based picker. Seismol. Res. Lett. 94, 1836–1847. https://doi.org/10.1785/0220220340.

Wang, R., Onyango, E.A., Schmandt, B., Worthington, L., 2024. Injection-induced basement seismicity beneath the Raton Basin: constraints from refined fault architectures and basin structure. Phil. Trans. R. Soc. A 382, 20230181. https://doi.org/10.1098/rsta.2023.0181.

Wei, Z., Chu, R., Xie, J., Bao, F., Zeng, S., Sheng, M., Zeng, Q., 2022. Crustal structure in the Weiyuan shale gas field, China, and its tectonic implications. Tectonophysics 837, 229449. https://doi.org/10.1016/j.tecto.2022.229449.

Wessel, P., Luis, J.F., Uieda, L., Scharroo, R., Wobbe, F., Smith, W.H.F., Tian, D., 2019. The generic mapping tools version 6. Geochem. Geophys. Geosyst. 20, 5556–5564. https://doi.org/10.1029/2019GC008515.

Wiemer, S., 2001. A software package to analyze seismicity: ZMAP. Seismol. Res. Lett. 72, 373–382. https://doi.org/10.1785/gssrl.72.3.373.

Yang, H., Zhu, L., Chu, R., 2009. Fault-plane determination of the 18 April 2008 Mount Carmel, Illinois, earthquake by detecting and relocating aftershocks. Bull. Seismol. Soc. Am. 99, 3413–3420. https://doi.org/10.1785/0120090038.

Yang, H., Zhou, P., Fang, N., Zhu, G., Xu, W., Su, J., Meng, F., Chu, R., 2020. A shallow shock: the 25 February 2019 ML 4.9 earthquake in the Weiyuan Shale Gas Field in Sichuan, China. Seismol. Res. Lett. 91, 3182–3194. https://doi.org/10.1785/0220200202.

Yang, Y., Yang, H., Zi, J., 2023. Stress transfer outpaces injection-induced aseismic slip and triggers seismicity. Sci. Rep. 13, 16626. https://doi.org/10.1038/s41598-023-43760-0.

Yi, G., Long, F., Liang, M., Zhao, M., Wang, S., 2020. Geometry and tectonic deformation of seismogenic structures in the Rongxian-Weiyuan-Zizhong region, Sichuan Basin: insights from focal mechanism solutions. Chin. J. Geophys. (in Chinese) 63, 3275–3291. https://doi.org/10.6038/cjg2020O0095.

Zhang, M., Ellsworth, W.L., Beroza, G.C., 2019. Rapid earthquake association and location. Seismol. Res. Lett. 90, 2276–2284. https://doi.org/10.1785/0220190052.

Zhang, M., Liu, M., Feng, T., Wang, R., Zhu, W., 2022a. LOC-FLOW: an end-to-end machine learning-based high-precision earthquake location workflow. Seismol. Res. Lett. 93, 2426–2438. https://doi.org/10.1785/0220220019.

Zhang, F., Wang, R., Chen, Y., Chen, Y., 2022b. Spatiotemporal variations in earthquake triggering mechanisms during multistage hydraulic fracturing in Western Canada. J. Geophys. Res. Solid Earth 127. https://doi.org/10.1029/2022JB024744 e2022JB024744.

Zhang, H., Tong, H., He, Y., Liu, Z., Zhou, Y., Zhang, P., Ren, X., Deng, C., Yin, Y., 2023. Structural analysis of superimposed deformation under oblique compression: a case study of the Weiyuan area, Sichuan Province. Acta Geol. Sin. 97, 1630–1640.

Zhang, W., Guo, R., Ji, L., Yang, H., Dai, K., Zi, J., Sun, H., 2024a. Shallow reverse moderate earthquakes in the Weiyuan Shale Gas Field, Sichuan Basin, China, related to hydraulic fracturing. Seismol. Res. Lett. 96, 1088–1101. https://doi.org/10.1785/0220230375.

Zhang, N., Zhou, L., Duan, M., Wen, Z., Wu, Q., 2024b. The temporal and spatial evolution characteristics of induced seismicity in the Changning shale gas field based on dense array. Sci. Rep. 14, 25287. https://doi.org/10.1038/s41598-024-77443-1.

Zhang, F., Chen, Y., Wang, R., Yu, H., Chen, H., Liu, F., Shi, X., 2025. Integrated analysis of seismic sources and structures: understanding earthquake clustering during hydraulic fracturing. J. Geophys. Res. Solid Earth 130. https://doi.org/10.1029/2024JB030008 e2024JB030008.

Zhao, M., Tang, L., Chen, S., Su, J., Zhang, M., 2021. Machine learning based automatic foreshock catalog building for the 2019 <i>M</i>_S6.0 Changning, Sichuan earthquake. Chin. J. Geophys. (in Chinese) 64, 54–66. https://doi.org/10.6038/cjg2021O0271.

Zhao, Y., Jiang, G., Lei, X., Xu, C., Zhao, B., Qiao, X., 2023. The 2021 Ms 6.0 Luxian (China) earthquake: Blind reverse-fault rupture in deep sedimentary formations likely induced by pressure perturbation from hydraulic fracturing. Geophys. Res. Lett. 50. https://doi.org/10.1029/2023GL103209 e2023GL103209.

Zhu, W., Beroza, G.C., 2018. PhaseNet: a deep-neural-network-based seismic arrival-time picking method. Geophys. J. Int. 216, 261–273. https://doi.org/10.1093/gji/ggy423.

Zi, J., Yang, H., Su, J., Chen, L., 2023. Structural constraints of induced earthquakes in the Weiyuan Shale Gas Field revealed by high-resolution body-wave tomography and earthquake relocation. Tectonophysics 864, 230007. https://doi.org/10.1016/j.tecto.2023.230007.

Zi, J., Yang, Y., Yang, H., Su, J., 2025. The 11-month precursory fault activation of the 2019 ML 5.6 earthquake in the Weiyuan shale gas field, China. Commun. Earth Environ. 6, 175. https://doi.org/10.1038/s43247-025-02151-1.